Preprints of the 21st IFAC World Congress (Virtual)
Berlin, Germany, July 12-17, 2020

Vision-integrated Navigation and Integrity Monitoring for Aircraft Final Approach

Yoko Watanabe *

* *ONERA - The French Aerospace Laboratory, Toulouse, France (e-mail:* Yoko.Watanabe@onera.fr*).*

Abstract: This paper proposes a tightly-integrated Vision/GNSS navigation system for aircraft final approach. It consists of: i) a Kalman filter-based state estimator which handles time-delayed vision measurements by using image-trigger signals of camera device, and ii) an integrity monitoring (IM) function for sensor fault detection and Protection Level calculation. The integrity monitoring function is founded on a batch-realization of Kalman filter. The paper introduces an IM reset mechanism which re-initializes a fault detector regularly without relying on the current state estimation result, in order to remove an influence of past undetected faults on the newly reset detector. The proposed navigation system is tested on real sensor measurements, acquired onboard an unmanned aircraft in flight, with simulated GNSS faults. The test results show an improvement in fault detectability as well as in navigation performance by adding onboard vision information to classical aircraft navigation system.

Keywords: Aircraft navigation, Integrity monitoring, Fault detection, Vision

1. INTRODUCTION

Increasing an autonomy level of the aircraft flight control system will alleviate the pilots' task and stress in handling critical situations, and hence is an important key to enhance civil aviation safety. In order to contribute towards it, a Europe-Japan collaborative research project called VISION [1] (Validation of Integrated Safety-enhanced Intelligent flight cONtrol) has been launched in 2016. This 3-year VISION project had objectives of developing and flight-evaluating advanced aircraft Guidance, Navigation and Control solutions that can automatically detect and overcome some critical flight situations.

As the project name signifies, one part of the VISION project focused on the onboard vision-aided aircraft navigation for airport approach. Recent large commercial airplanes are equipped with onboard cameras, which are used to augment pilot's situational awareness for obstacle clearance during taxiing. Although their current usage is still very limited to cockpit display for pilot aid, these sensors have a significant potential to provide useful information to the aircraft flight control system during on-ground and near-ground operations.

An idea of using onboard vision in the aircraft approach and landing navigation is very spontaneous, and have been addressed in past projects. In the EU-funded PEGASE project, the position- and image-based visual servoing algorithms for final approach guidance were proposed[T.Goncalves et al. (2010), L.Coutard et al. (2011)]. The French nation-funded Visioland project proposed online estimation algorithms of the aircraft glide path deviation by using image features[V.Gibert et al. (2015)].

These work use onboard vision as an *alternative* navigation sensor to the classical ones such as GNSS (Global Navigation Satellite Systems) or ILS (Instrument Landing System), but do not cope with them. The German national-funded C2Land project has proposed a vision-augmented automatic landing system, and flight demonstrated it on a real aircraft[C.Tonhäuser et al. (2015), M.E.Kügler et al. (2019)]. Integrity monitoring (IM) of navigation solution is a requirement for civil aviation application. From measurement redundancy, the IM function performs Fault Detection and Exclusion (FDE) as well as Protection Level (PL) calculation. Instead of using vision information directly in navigation filter, the C2Land system uses it as a dissimilar reference in integrity monitoring of the conventional loosely-coupled GNSS/INS navigation solution.

In our VISION project, a tightly-coupled GNSS/Vision/INS navigation system for aircraft final approach has been developed, and augmented with an IM function. This VISION system uses onboard vision as an *additional* but not *alternative* sensor for extending the aircraft navigation capability in case of GNSS or ILS failures. The proposed Kalman filter-based estimator design has a specificity in its way to handle a non-negligible time delay of vision-based measurements due to image processing. It makes use of image-trigger signals (originally for sending to camera devices) to notify the navigation filter a time instant of image acquisition. This enables the filter to anticipate and prepare for a future arrival of vision measurements,and hence to incorporate efficiently the time-delayed measurements[Y.Watanabe et al. (2019)]. Then, the IM function is founded on a batch-realization of this time-delayed

⋆ This work has received funding from the European Union's Horizon 2020 research and innovation programme under grant agreement No. 690811 and the Japan New Energy and Industrial Technology Development Organization under grant agreement No. 062800, as a part of the EU/Japan joint research project entitled "'Validation of Integrated Safety-enhanced Intelligent flight cONtrol (VISION)."'

[1] http://w3.onera.fr/h2020_vision

measurement KF framework. This paper introduces an IM reset mechanism which re-initializes a fault detector without relying on the current navigation solution. In this way, a bias issued by past undetected faulty measurements can be removed from the newly reset detector.

The proposed system has been tested on real sensor data, acquired onboard a fixed-wing UAV on a runway approach trajectory, with simulated GNSS faults.

2. NAVIGATION FILTER DESIGN

2.1 Reference frames

Different reference frames are defined and used in the navigation filter design. Besides the conventionally used ones (WGS84, ECEF, NED, aircraft body), the following frames are defined.

Runway frame (RWY): A Cartesian coordinate system fixed on Earth at a runway threshold center point, with its X-axis aligned with the runway axis, and Z-axis normal downward to the runway plane.

Camera frame: A Cartesian coordinate system fixed on a camera, with its origin at the optical center, its Z-axis aligned with the optical axis and X-axis with the image horizontal to the right.

Image frame: A 2D pixel-coordinate system fixed on a camera's image plane with its origin at a left-top corner.

2.2 Aircraft navigation state kinematics

Let $\boldsymbol{x}$ be a navigation state vector defined by

$$\boldsymbol{x} = \begin{bmatrix} \boldsymbol{X}^T & \boldsymbol{V}^T & \boldsymbol{b}_a^T & P_0 & \boldsymbol{\tau}^T = [\,\tau & v_\tau\,] \end{bmatrix}^T \tag{1}$$

where $\boldsymbol{X}$ and $\boldsymbol{V}$ are the aircraft position and velocity in the NED frame, $\boldsymbol{b}_a$ is an accelerometer bias in the aircraft body frame, P_0 is a pressure adjusted to a standard atmosphere at sea level and $\boldsymbol{\tau}$ is a clock offset of a GNSS receiver and its changing rate. Then its time-discretized kinematics is given as below.

$$\boldsymbol{x}_{k+1} = \boldsymbol{x}_k + \begin{bmatrix} \boldsymbol{V}_k\Delta t + \frac{1}{2}\boldsymbol{a}_k\Delta t^2 \\ \boldsymbol{a}_k\Delta t \\ \boldsymbol{\nu}_{b_a k} \\ \boldsymbol{\nu}_{P_0 k} \\ \begin{bmatrix} v_{\tau k}\Delta t \\ 0 \end{bmatrix} + \boldsymbol{\nu}_{\tau k} \end{bmatrix} \tag{2}$$

where $\boldsymbol{a}_k = R(\boldsymbol{q}_k)(\boldsymbol{a}_{IMU\,k} - \boldsymbol{b}_{a\,k} - \boldsymbol{\nu}_{a\,k}) + \boldsymbol{g}$ is the aircraft acceleration in the NED frame, derived from the accelerometer measurement. All the $\boldsymbol{\nu}$ terms are independent zero-mean Gaussian noises. The aircraft attitude quaternion $\boldsymbol{q}_k$ and angular velocity $\boldsymbol{\omega}_k$ are estimated by an attitude filter. For simplicity of presenting the filter design and IM concept, this paper assumes a perfect attitude estimation [2]. Let $\boldsymbol{u}_k = R(\boldsymbol{q}_k)\boldsymbol{a}_{IMU\,k} + \boldsymbol{g}$. (2) can be rewritten in a linear form.

$$\boldsymbol{x}_{k+1} = \Phi_k\boldsymbol{x}_k + B\boldsymbol{u}_k + G_k\boldsymbol{\nu}_k \tag{3}$$

where Φ_k and G_k depend on the attitude $\boldsymbol{q}_k$.

[2] One can easily incorporate the attitude estimation error by including it into a process/measurement noise. It was done so in evaluation tests with real sensor data, presented later in this paper.

2.3 Sensor measurements

GNSS: Let $\boldsymbol{X}_{GNSS\,k}$ and $\boldsymbol{V}_{GNSS\,k}$ be the receiver position and velocity in the NED frame. In GNSS tight-coupling, a set of pseudo-range measurements of the visible satellites is used as a position measurement. The i-th satellite pseudo-range can be modeled by

$$z_{\rho_k^i} = \|\boldsymbol{X}_{GNSS_k}^{ECEF} - \boldsymbol{X}_{SAT_k^i}^{ECEF}\| + c(\tau_k - \tau_k^i) + \xi_{\rho_k^i}$$

where c is a light speed, $\boldsymbol{X}_{SAT_k^i}^{ECEF}$ and τ_k^i (provided by the receiver) are a position of the i-th satellite in the ECEF frame and its clock bias. $\xi_{\rho_k^i}$ is a zero-mean Gaussian noise which includes errors from different sources (satellite clock and ephemeris errors, compensation errors in ionosphereic and tropospheric signal delays, multipath effects). The velocity measurement is given directly in the NED frame.

$$\boldsymbol{z}_{V\,k} = \boldsymbol{V}_{GNSS\,k} + \boldsymbol{\xi}_{V_k}$$

Barometer: A barometer gives an atmospheric pressure measurement which is related to the aircraft altitude.

$$z_{P\,k} = P_{0_k} e^{\frac{gM}{R_0 T_0}(Z_k - h_0)} + \xi_{P\,k}$$

where h_0 is the height above MSL of the NED frame origin. M, R_0 and T_0 are the known constants of the standard atmosphere.

Vision sensors: In this work, two independent onboard vision systems based on monocular- and stereo-cameras are considered. The both systems detect runway features shown in Fig.1, and calculate the camera's 6D pose in the RWY frame from them. Let $\boldsymbol{X}_{THD_k}^{CAM}$ be the runway threshold center point in the Camera frame.

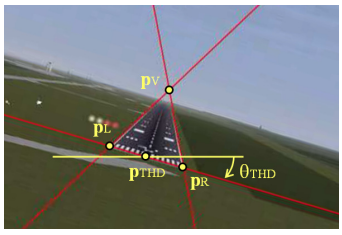

Fig. 1. Runway features to be detected by image processing

The stereo-vision system measures its pixel-coordinates $\boldsymbol{p}_{THD}$ and disparity d_{THD}. Given camera parameters (focal length $f_{x,y}$, image center $c_{x,y}$ and stereo-baseline L), the stereo-vision measurement is modeled as follows.

$$\boldsymbol{z}_{THD\,k} = \frac{1}{Z_{THD_k}^{CAM}} \begin{bmatrix} f_x & 0 & c_x & 0 \\ 0 & f_y & c_y & 0 \\ 0 & 0 & 0 & f_x \end{bmatrix} \begin{bmatrix} \boldsymbol{X}_{THD_k}^{CAM} \\ L \end{bmatrix} + \boldsymbol{\xi}_{THD\,k}$$

The monocular-vision system resolves a scale ambiguity by assuming a knowledge on the runway width. Our navigation filter design treats the reconstructed camera position in the RWY frame as a monocular-vision measurement (i.e., loose-coupling).

$$\boldsymbol{z}_{X\,k} = \boldsymbol{X}_{CAM_k}^{RWY} + \boldsymbol{\xi}_{X\,k} = -R(\boldsymbol{q}_{CAM/RWY})X_{THD_k}^{CAM} + \boldsymbol{\xi}_{X\,k}$$

where $\boldsymbol{q}_{CAM/RWY}$ is the Camera frame orientation w.r.t. the RWY frame. It should be noted that a covariance of the measurement error $\boldsymbol{\xi}_{X\,k}$ can be derived from the image feature detection error covariance in pixels. In particular, it quadratically increases with image depth $Z_{THD_k}^{CAM}$.

2.4 Kalman filter with time-delayed measurement

An Extended Kalman filter (EKF) is applied to estimate the navigation state $\boldsymbol{x}_k$ from the sensor measurements listed above. For the non-delayed measurements, the nominal EKF prediction and correction steps are applied.

The vision measurements arrive with a non-negligible time delay due to image processing, and this time-delay should be taken into account in the filter design. A common way is to stock data histories for a certain time horizon, and to re-run the KF processes from a time of the measurement up to the current time as if it arrived without delay. To avoid a need of data storage, this paper proposes to use image-trigger signals to notify the image acquisition time in advance before the corresponding measurement arrives.

Let k_i be a time step at which the i-th KF correction step is performed, i.e., the i-th measurement $\boldsymbol{z}_{k_i}$ is delivered. It may have a time delay, and let $m_i(\leq k_i)$ be a time step when that measurement was taken (Fig.2). Let $\hat{\boldsymbol{x}}^+_{m_i}$ be a back-propagated estimation state at m_i from the lastly updated estimate $\hat{\boldsymbol{x}}_{k_{i-1}}$. Then, the following EKF correction makes a direct correction on the current predicted state[T.D.Larsen et al. (1998)].

$$\begin{cases} \hat{\boldsymbol{x}}_{k_i} = \hat{\boldsymbol{x}}^-_{k_i} + K_{k_i}\Delta\boldsymbol{z}_{k_i} \\ P_{k_i} = P^-_{k_i} - K_{k_i}H_{k_i}P_{m_ik_i} \\ K_{k_i} = P^T_{m_ik_i}H^T_{k_i}(H_{k_i}P^+_{m_i}H^T_{k_i} + R_{k_i})^{-1} \end{cases} \tag{4}$$

where $\Delta\boldsymbol{z}_{k_i} = \boldsymbol{z}_{k_i} - \boldsymbol{h}_{k_i}(\hat{\boldsymbol{x}}^+_{m_i})$ and $H_{k_i} = \partial\boldsymbol{h}_{k_i}(\boldsymbol{x})/\partial\boldsymbol{x}$ evaluated at $\hat{\boldsymbol{x}}^+_{m_i}$. $P^+_{m_i}$ is an error covariance of the back-propagated state and $P_{m_ik_i} = \mathbb{E}[\tilde{\boldsymbol{x}}^+_{m_i}\tilde{\boldsymbol{x}}^{-T}_{k_i}]$ is its correlation with the current prediction error. Hence now, what we need to do is to derive the back-propagated state $\hat{\boldsymbol{x}}^+_{m_i}$, its error covariance and correlation matrices $P^+_{m_i}$ and $P_{m_ik_i}$.

2.5 Back-propagation

As Fig.2 illustrates, let $k_{j-1} \leq m_i < k_j$, $j \leq i$. If the navigation filter receives an image-trigger signal at the time step m_i, it is possible to perform the back-propagation (BP) process, needed for (4), forward in time until the measurement arrives at k_i. At the time step m_i, the BP process is initialized as below.

$$\hat{\boldsymbol{x}}^+_{m_i} = \hat{\boldsymbol{x}}^-_{m_i}, \quad \Gamma_i = I, \quad \Delta Q_i = O, \quad \delta Q_i = O$$

Then, the two processes are iterated to update them:

BP prediction: At each time step $\ell+1$ when the KF prediction is performed,

$$\begin{cases} \Gamma_i = \Phi_\ell\Gamma_i \\ \Delta Q_i = \Phi_\ell\Delta Q_i\Phi^T_\ell + G_\ell Q_\ell G^T_\ell \\ \delta Q_i = \Phi_\ell\delta Q_i\Phi^T_\ell \end{cases} \tag{5}$$

BP update: At each time step k_ℓ $(j \leq \ell < i)$ when the KF correction is performed (followed to the prediction),

$$\begin{cases} \hat{\boldsymbol{x}}^+_{m_i} = \hat{\boldsymbol{x}}^+_{m_i} - \Gamma^{-1}_i K_{k_\ell}\Delta\boldsymbol{z}_{k_\ell} \\ \delta Q_i = (I - K_{k_\ell}\bar{H}_{k_\ell})\delta Q_i + \gamma K_{k_\ell}\bar{H}_{k_\ell}(\Delta Q_i - \Delta Q_\ell) \end{cases} \tag{6}$$

where $\bar{H}_{k_\ell} = H_{k_\ell}\Gamma^{-1}_\ell$. $\gamma = 0$ when $m_\ell < m_i$, and 1 otherwise. Finally at a time step k_i when the vision measurement arrives, the back-propagated state $\hat{\boldsymbol{x}}^+_{m_i}$ is already ready to be used for computing the measurement residual $\Delta\boldsymbol{z}_{k_i}$. The covariance and correlation matrices in (4) can be given by

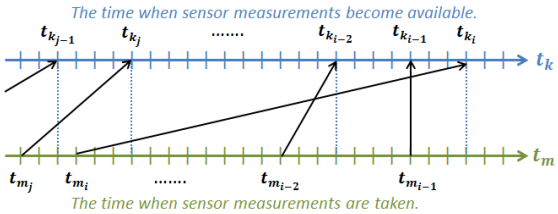

Fig. 2. Timelines for delayed sensor measurements

$$\begin{cases} P^+_{m_i} = \Gamma^{-1}_i\bar{P}^+_{m_i}\Gamma^{-T}_i, & \bar{P}^+_{m_i} = (P^-_{k_i} - \Delta Q_i + \delta Q_i + \delta Q^T_i) \\ P_{m_ik_i} = \Gamma^{-1}_i\bar{P}_{m_ik_i}, & \bar{P}_{m_ik_i} = (P^-_{k_i} - \Delta Q_i + \delta Q^T_i) \end{cases}$$

But with $\bar{H}_{k_i}$, (4) can be implemented as below.

$$\begin{cases} \hat{\boldsymbol{x}}_{k_i} = \hat{\boldsymbol{x}}^-_{k_i} + K_{k_i}\Delta\boldsymbol{z}_{k_i} \\ P_{k_i} = P^-_{k_i} - K_{k_i}\bar{H}_{k_i}\bar{P}_{m_ik_i} \\ K_{k_i} = \bar{P}^T_{m_ik_i}\bar{H}^T_{k_i}(\bar{H}_{k_i}\bar{P}^+_{m_i}\bar{H}^T_{k_i} + R_{k_i})^{-1} \end{cases} \tag{7}$$

The details of this time-delayed measurement KF approach are provided in [Y.Watanabe et al. (2019)].

3. INTEGRITY MONITORING

The vision-integrated estimator in Section 2 is augmented with an Integrity Monitoring (IM) function for fault detection and Protection Level (PL) calculation, which is a requirement in civil aviation. This paper applies a residual-based LS-RAIM (Least-Square Receiver Autonomous Integrity Monitoring) algorithm, well-developed for GNSS receivers, to a batch-realization of the Kalman filter [M.Joerger and B.Pervan (2013)].

3.1 Batch realization of Kalman filter

Consider that the navigation filter is initialized at a time step k_0 with $\hat{\boldsymbol{x}}_{k_0}$ and P_{k_0}. Then the time-delayed EKF process (Section 2) from k_0 to k can be re-written in a batch realization form with a zero-mean Gaussian noise $\boldsymbol{v}_K \sim \mathcal{N}(\boldsymbol{0}, V_K)$ and a bias fault vector $\boldsymbol{f}_K$.

$$\boldsymbol{\delta z}_K = \mathcal{H}_K\boldsymbol{\delta x}_K + \boldsymbol{v}_K + \mathcal{T}_K\boldsymbol{f}_K \tag{8}$$

At time k_0, the batch realization is initialized with known $\boldsymbol{\delta z}_{K_0} = \boldsymbol{0}$ and $\mathcal{H}_{K_0} = \mathcal{T}_{K_0} = I$, and unknown

$$\boldsymbol{\delta x}_{K_0} = \tilde{\boldsymbol{x}}_{k_0}, \quad \boldsymbol{v}_{K_0} = -(\tilde{\boldsymbol{x}}_{k_0} - \mathbb{E}[\tilde{\boldsymbol{x}}_{k_0}]), \quad \boldsymbol{f}_{K_0} = -\mathbb{E}[\tilde{\boldsymbol{x}}_{k_0}]$$

where $\tilde{\boldsymbol{x}}_{k_0}$ is the initial estimation error. Then (8) is incrementally defined: When the KF prediction is performed at a time step $k+1$,

$$\begin{aligned} \boldsymbol{\delta z}_{K+1} &= \mathcal{H}_{K+1}\boldsymbol{\delta x}_{K+1} + \boldsymbol{v}_{K+1} + \mathcal{T}_{K+1}\boldsymbol{f}_{K+1} \\ &= \begin{bmatrix} \mathcal{H}_K & O \\ [O \quad \Phi_k] & -I \end{bmatrix}\begin{bmatrix} \boldsymbol{\delta x}_K \\ \tilde{\boldsymbol{x}}^-_{k+1} \end{bmatrix} + \begin{bmatrix} \boldsymbol{v}_K \\ G_k\boldsymbol{\nu}_k \end{bmatrix} + \begin{bmatrix} \mathcal{T}_K \\ O \end{bmatrix}\boldsymbol{f}_K \end{aligned}$$

where $\boldsymbol{\delta z}^T_{K+1} = [\,\boldsymbol{\delta z}^T_K \quad \boldsymbol{0}^T\,]$ when there was no KF correction at the previous time k, and otherwise,

$$\boldsymbol{\delta z}^T_{K+1} = [\,\boldsymbol{\delta z}^T_K \quad (\Phi_k K_k\Delta\boldsymbol{z}_k)^T\,].$$

When the KF correction is performed at $k+1 = k_i$ after the prediction, it is further updated to

$$\boldsymbol{\delta z}_{K+1} = \begin{bmatrix} \boldsymbol{\delta z}_{K+1}^T & (\Delta \boldsymbol{z}_{k_i} + H_{k_i} \sum_{\ell=j}^{i-1} \Phi_{m_i,k_\ell}^{-1} K_{k_\ell} \Delta \boldsymbol{z}_{k_\ell})^T \end{bmatrix}^T$$
$$= \begin{bmatrix} \mathcal{H}_{K+1} \\ H_{k_i} E_{m_i}^T \end{bmatrix} \boldsymbol{\delta x}_{K+1} + \begin{bmatrix} \boldsymbol{v}_{K+1} \\ \boldsymbol{\xi}_{k_i} \end{bmatrix} + \begin{bmatrix} \mathcal{T}_{K+1} & O \\ O & I \end{bmatrix} \begin{bmatrix} \boldsymbol{f}_{K+1} \\ \boldsymbol{f}_{k_i} \end{bmatrix}$$

where Φ_{m_i,k_ℓ} is a state transition matrix from m_i to k_ℓ, and $E_{m_i}^T$ is a matrix to extract the m_i-th state. $\boldsymbol{f}_{k_i}$ is a fault vector of the sensor measurement obtained at k_i.

3.2 Residual-based LS-RAIM algorithm

This paper applies the residual-based LS-RAIM algorithm [M.Joerger et al. (2014)] to (8). The full-state $\boldsymbol{\delta x}_K$ is observable from the measurement $\boldsymbol{\delta z}_K$ because the following observability matrix has full-rank.

$$\mathcal{O}_K^T = [\, I \quad (H_{k_1}\Phi_{k_0,m_1})^T \quad \cdots \quad (H_{k_i}\Phi_{k_0,m_i})^T \,]$$

Then the LS-estimate of $\boldsymbol{\delta x}_K$ is given by

$$\boldsymbol{\delta \hat{x}}_{K|K} = S_K \boldsymbol{\delta z}_K = \boldsymbol{\delta x}_K + S_K(\boldsymbol{v}_K + \mathcal{T}_K \boldsymbol{f}_K) \tag{9}$$

where $\mathcal{P}_{K|K} = (\mathcal{H}_K^T V_K^{-1} \mathcal{H}_K)^{-1}$ and $S_K = \mathcal{P}_{K|K}\mathcal{H}_K^T V_K^{-1}$. Its error $\boldsymbol{\delta \tilde{x}}_{K|K}$ follows a normal distribution $\mathcal{N}(-S_K\mathcal{T}_K\boldsymbol{f}_K, \mathcal{P}_{K|K})$. Note that the current state estimate is equivalent to that of the KF: $\hat{\boldsymbol{x}}_k = \hat{\boldsymbol{x}}_k^- + \boldsymbol{\delta \hat{x}}_{k|K}$, $P_k = \mathcal{P}_{k|K}$.

Fault detector: By using a residual vector $\boldsymbol{r}_{K|K} = \boldsymbol{\delta z}_K - \mathcal{H}_K \boldsymbol{\delta \hat{x}}_{K|K}$, the fault detector is defined by

$$q_K^2 = \boldsymbol{r}_{K|K}^T V_K^{-1} \boldsymbol{r}_{K|K} \sim \chi^2(m_K - n_K, \lambda_K^2) \tag{10}$$

which follows a χ^2-distribution with non-centrality $\lambda_K^2 = \boldsymbol{f}_K^T \mathcal{T}_K^T V_K^{-1}(I - \mathcal{H}_K S_K)\mathcal{T}_K \boldsymbol{f}_K$. m_K and n_K are dimensions of $\boldsymbol{\delta x}_K$ and $\boldsymbol{\delta z}_K$ respectively. The detection threshold $q_{T_K}^2$ can be determined by limiting the false alarm probability (under fault-free hypothesis F_0 where $\boldsymbol{f}_K = \boldsymbol{0}$) by a given continuity risk requirement P_{CR}.

$$Pr(q_K^2 \geq q_{T_K}^2 | F_0) Pr(F_0) \leq Pr(q_K^2 \geq q_{T_K}^2 | F_0) = P_{CR} \tag{11}$$

Integrity risk requirement: Let $\boldsymbol{y}_{k|K} = A^T \boldsymbol{x}_k$ be a current state-of-interest, for which integrity should be monitored. For example, $\boldsymbol{y}$ could be the horizontal position or altitude. Its estimation error follows a normal distribution: $\tilde{\boldsymbol{y}}_{k|K} \sim \mathcal{N}(-A_k^T S_K T_K \boldsymbol{f}_K, A^T P_{k|K} A)$, where $A_k^T = A^T E_k^T$ with the k-th state extraction matrix. The integrity risk under each fault mode F_n is defined as the Hazardous Misleading Information (HMI) probability:

$$\begin{aligned} P_{I_K}(F_n) &= Pr(\|\tilde{\boldsymbol{y}}_{k|K}\| > AL, q_K^2 < q_{T_K}^2 | F_n) \\ &= Pr(\|\tilde{\boldsymbol{y}}_{k|K}\| > AL | F_n) Pr(q_K^2 < q_{T_K}^2 | F_n) \end{aligned} \tag{12}$$

where AL is a given Alert Limit. (12) needs to be bounded by a given allocated integrity risk requirement P_{IR_n} for every fault hypothesis F_n, i.e., $P_{I_K}(F_n) \leq P_{IR_n}$.

Worst-case fault: The worst-case fault $\boldsymbol{f}_n^* \in F_n$ is a fault vector maximizing its integrity risk:

$$\boldsymbol{f}_n^* = \arg \max_{\boldsymbol{f}_n \in F_n} P_{I_K}(\boldsymbol{f}_n)$$

where the fault vector affects on the non-centrality of the detector and the mean of the estimation error. It is actually the one maximizing the failure mode slope:

$$g_K^2(\boldsymbol{f}_K = \boldsymbol{f}_n) = \frac{\boldsymbol{f}_{NZ_n}^T \tilde{\mathcal{T}}_K^T S_K^T A_k A_k^T S_K \tilde{\mathcal{T}}_K \boldsymbol{f}_{NZ_n}}{\boldsymbol{f}_{NZ_n}^T \tilde{\mathcal{T}}_K^T V_K^{-1}(I - \mathcal{H}_K S_K)\tilde{\mathcal{T}}_K \boldsymbol{f}_{NZ_n}} \tag{13}$$

where $\tilde{\mathcal{T}}_K = \mathcal{T}_K C_n$, with a faulty sensor selection matrix $C_n = blkdiag(C_{n_0}, C_{n_1}, \cdots, C_{n_i})$ which extracts the non-zero elements $\boldsymbol{f}_{NZ_n} = C_n^T \boldsymbol{f}_n$ from the fault vector.

Complementary, let $\bar{C}_n$ and $\bar{C}_{n_i}$ be non-faulty sensor selection matrices ($\bar{C}_n^T \boldsymbol{f}_n = \boldsymbol{0}$). For fault detection, the full-state still needs to be observable only with the non-faulty measurements. That is, the following sub-set observability matrix must have a full rank.

$$\mathcal{O}_{K_n}^T = [\, \bar{C}_{n_0} \quad \bar{C}_{n_1}(H_{k_1}\Phi_{k_0,m_1})^T \quad \cdots \quad \bar{C}_{n_i}(H_{k_i}\Phi_{k_0,m_i})^T \,]$$

When $\mathcal{O}_{K_n}$ has full-rank, the matrix $\tilde{\mathcal{T}}_K^T V_K^{-1}(I - H_K S_K)\tilde{\mathcal{T}}_K$ in the denominator of (13) is invertible. Let M_K denote its inverse. Then, the failure mode slope is upper-bounded.

$$\begin{aligned} g_K^2(\boldsymbol{f}_K = \boldsymbol{f}_n) &\leq \lambda_{max}(M_K^{\frac{1}{2}} \tilde{\mathcal{T}}_K^T S_K^T A_k A_k^T S_K \tilde{\mathcal{T}}_K M_K^{\frac{1}{2}}) \\ &= \lambda_{max}(A_k^T S_K \tilde{\mathcal{T}}_K M_K \tilde{\mathcal{T}}_K^T S_K^T A_k) \\ &= \lambda_{max}(A^T \tilde{M}_k A) = \lambda_{max} \end{aligned} \tag{14}$$

where $\lambda_{max}(\cdot)$ returns a maximum eigenvalue. Let $\boldsymbol{v}_{max}$ be the unit eigenvector of $A^T \tilde{M}_k A$ corresponding to λ_{max}. Then the worst-case fault $\boldsymbol{f}_n^*$ can be determined as below.

$$\boldsymbol{f}_n^* = C_n \boldsymbol{f}_{NZ_n}^* = \frac{f_n^*}{\sqrt{\lambda_{max}}} C_n M_K \tilde{\mathcal{T}}_K^T S_K^T A_k \boldsymbol{v}_{max}$$

When $\boldsymbol{f}_K = \boldsymbol{f}_n^*$, the detector q_K^2 and the state-of-interest estimation error $\tilde{\boldsymbol{y}}_{k|K}$ will follow:

$$\begin{cases} q_K^2(\boldsymbol{f}_K = \boldsymbol{f}_n^*) \sim \mathcal{N}(m_K - n_K, {f_K^*}^2) \\ \tilde{\boldsymbol{y}}_{k|K}(\boldsymbol{f}_K = \boldsymbol{f}_n^*) \sim \mathcal{N}(-f_K^* \sqrt{\lambda_{max}} \boldsymbol{v}_{max}, A^T P_{k|K} A) \end{cases} \tag{15}$$

The fault magnitude f_n^* is the one maximizing the integrity risk under (15), and can be found by a line search algorithm. Since (12) is upper-bounded by this worst-case fault integrity risk, the integrity requirement can be conservatively guaranteed if, for all F_n,

$$Pr(\|\tilde{\boldsymbol{y}}_{k|K}\| > AL, q_K^2 < q_{T_K}^2 | \boldsymbol{f}_K = \boldsymbol{f}_n^*) \leq P_{IR_n} \tag{16}$$

Protection Level: PL is defined by the minimum AL respecting the integrity risk requirement. That is, when no detection, the estimation error is guaranteed to lie within the PL-bound for a probability of $(1 - P_{IR})$. By using (16) under (15) for each fault mode F_n, the PL can be conservatively approximated by a solution of

$$Pr(\|\tilde{\boldsymbol{y}}_{k|K}\| > PL_n, q_K^2 < q_{T_K}^2 | \boldsymbol{f}_K = \boldsymbol{f}_n^*) = P_{IR_n}$$

By applying the triangle inequality to $\|\tilde{\boldsymbol{y}}_{k|K}\|$, the PL can be further approximated as follows.

$$PL(F_n) = PL_n = \sigma_n + |f_n^*| \sqrt{\lambda_{max}} \tag{17}$$

where, for $\Delta\tilde{\boldsymbol{y}}_{k|K} \sim \mathcal{N}(\boldsymbol{0}, A^T P_{k|K} A)$, σ_n satisfies

$$Pr(\|\Delta\tilde{\boldsymbol{y}}_{k|K}\| \leq \sigma_n) = 1 - \frac{P_{IR_n}}{Pr(q_K^2 < q_{T_K}^2 | \boldsymbol{f}_K = \boldsymbol{f}_n^*)}$$

For the fault-free mode F_0, we have $\boldsymbol{f}_0^* = \boldsymbol{0}$ and hence $PL_0 = \sigma_0$ with $Pr(q_K^2 < q_{T_K}^2 | F_0) = 1 - P_{CR}$.

Once the PLs are obtained for all the fault modes, the global PL can be determined by $PL_K = \max\{PL_n\}$.

3.3 Implementation

For the IM purpose, all what we need to track are the detector value q_K^2 in (10), the degree-of-freedom $m_K - n_K$ of its χ^2-distribution, and the matrix $\tilde{M}_k$ in (14) for calculating the worst-case fault. These can be computed by a recursively manner by using the EKF results.

The fault detector and the degree-of-freedom are set to zero at the initial time step k_0. Their values are incremented upon each KF correction (at time step $k+1 = k_i$):

$$\begin{cases} (m_{K+1} - n_{K+1}) = (m_K - n_K) + m_{k_i} \\ q_{K+1}^2 = q_K^2 + \Delta \boldsymbol{z}_{k_i}^T (H_{k_i} \mathcal{P}_{m_i}^+ H_{k_i}^T + R_{k_i})^{-1} \Delta \boldsymbol{z}_{k_i} \end{cases} \quad (18)$$

The matrix $\tilde{M}_k$, for a fault mode F_n, can be written by

$$\tilde{M}_k = E_k^T (\bar{M}_{K|K} - \mathcal{P}_{K|K}) E_k = \bar{M}_{k|K} - \mathcal{P}_{k|K} \quad (19)$$

The matrix $\bar{M}_{K|K}$ corresponds to the error covariance of the LS-estimate with a non-faulty sub-set of the measurements selected by $\bar{C}_n$. In consequence, $\bar{M}_{k|K}$ is the error covariance of the sub-set Kalman filter, and $\tilde{M}_k$ is equivalent to its difference from that of the full-set KF, like the Solution Separation approach [M.Joerger et al. (2014)]. Therefore, in the IM process, one full-set Kalman filter (under fault-free hypothesis F_0) and a bank of the sub-set Kalman filters under all the other fault modes should be ran in parallel.

3.4 IM reset mechanism

As time step proceeds, the detector value and the degree-of-freedom keep increasing by (18), and more critically, the fault mode set augments considerably. To address this issue, this paper introduces a new IM reset mechanism which runs several IM processes in parallel over different time windows (Figure 3). Suppose that we reset and initialize an IM process at k_0. This IM process becomes valid only after the time step k when the sub-set observability matrices $\mathcal{O}_{K_n}$ for all F_n will have full-rank. In our work, the initial estimation bias $\mathbb{E}[\tilde{\boldsymbol{x}}_{k_0}]$ is included in a fault vector. Hence, for fault modes with $C_{n_0} = I$ (or $\bar{C}_{n_0} = O$) assuming the non-zero initial estimation bias, it is not immediate for its $\mathcal{O}_{K_n}$ to have full-rank. Hence, the time window duration and the reset timing should be determined carefully by the sensor frequencies and the fault hypotheses, such that there is at least one valid IM process at any time instant.

A key idea of the proposed IM reset mechanism is that it assumes $C_{n_0} = I$ by default even in the full-set Kalman filter. It means that each IM process is re-initialized without relying on the current estimation result from the main navigation filter. By doing so, we can remove an influence (bias) of past undetected faults on the newly reset detector, and hence ensure an existence of at least one non-faulty sub-set filter in the IM process at any time instant. It makes possible to detect even a slowly drifting bias which is in general very difficult to capture. In practice, we still use the current estimate $\hat{\boldsymbol{x}}_{k_0}$ from the main navigation filter for initializing the KFs in the IM process, but with a sufficiently largely-inflated error covariance matrix instead of P_{k_0} from the main filter.

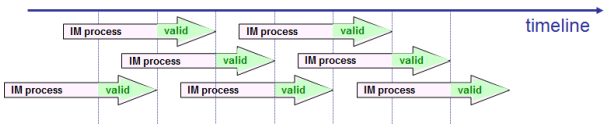

Fig. 3. IM reset mechanism

4. EXPERIMENT RESULTS

4.1 K50 UAV platform and Onboard vision sensors

The proposed Vision/GNSS navigation system has been tested in open-loop simulations with real sensor data acquired in flight experiments using a fixed-wing UAV platform, called K50-Advanced (Fig.4). It is equipped with the basic navigation sensors (IMU–50 Hz, GPS–20 Hz and Barometer–1.89 Hz), as well as with the two vision systems: long-range stereo-vision and monocular-vision developed by RICOH company and MTA SZTAKI respectively in VISION project. Fig.5 shows an example of the depth image constructed by the RICOH's stereo-vision during flight. The stereo-vision system outputs the navigation data at 15 (Hz) with about 105 (msec) of delay, while the monocular-vision at 10 (Hz) with 75 (msec) of delay. The both systems are designed to send their image-trigger signals to the navigation filter so that it can apply the time-delayed EKF approach presented in Section 2.

Fig. 4. K50 UAV with on-board cameras

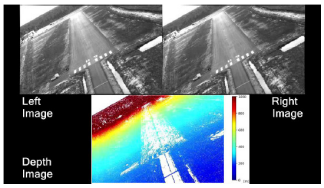

Fig. 5. Depth image from the RICOH stereo-camera

4.2 Fault modes and IM settings

In this test, single frequency (L1) GPS pseudo-range measurements are used. A single satellite fault is assumed in the IM process. A fault is simulated by introducing a fault percentage on the ionospheric delay correction signal on one selected satellite (PRN 12). As the barometer measurement actually had a time delay which was also estimated in the navigation filter, at least four pseudo-range, two velocity and two barometer measurements are needed for full-state observability. Based on that, we chose to run three IM processes, with the window length of 3 times barometer sampling time, in parallel. The IM reset is performed upon each barometer measurement reception.

The IM parameters used in this paper correspond to the APV-II aircraft approach requirements [ICAO (2005)]: $HAL = 40$ (m), $VAL = 20$ (m), $P_{CR} = 1.3333 \times 10^{-7}$ (/h), $P_{IR} = 4.8 \times 10^{-6}$ (/h), and a single satellite failure probability $P(F_n) = 1.16 \times 10^{-5}$ (/h).

4.3 Results

First, a step fault percentage is introduced. Fig.6 compares the results of Time-to-Alert (TTA) after the fault occurrence for different sensor sets used in the navigation filter and for different fault percentages. The fault detectability

is improved from 80% fault (3.3m bias, in blue solid) to 50% fault (2m bias, in red solid) by adding the two vision systems. It also shortens the detection time. Fig.7 shows the horizontal and vertical PLs for the case of 100% fault percentage introduced at t=2 (sec). These PLs are reduced compared to those calculated by the snap-shot LS-RAIM, and hence the navigation solution availability is also improved by adding onboard vision.

Fig.8 plots evolution of the detector values calculated by the full-set filter (left) and by the sub-set filters for each fault mode (right) when introducing 70% fault percentage. The figure compares the results of the filter configurations without (top) and with (bottom) the vision systems. When using onboard vision, the fault was detected after 1.28 (sec) when the full-set filter detector (blue) exceeds its threshold (red). The right plots show that only the detector calculated by the sub-set filter which excludes the right faulty satellite measurement (PRN12) follows a centralized χ^2-distribution (blue), and this fact can be used for fault mode identification.

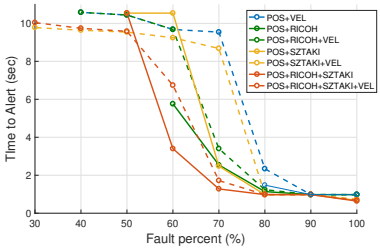

Fig. 6. Time-to-Alert vs. Fault percentages

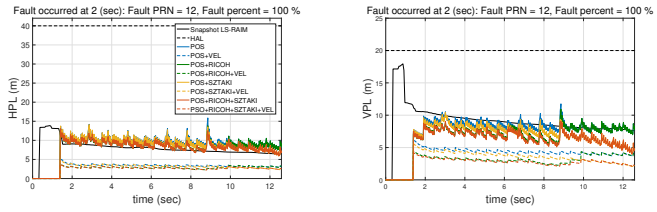

Fig. 7. Horizontal (left) and Vertical (right) PLs

Similar results were obtained when introducing a ramp fault. In the case of 20 (%/sec) fault percentage slope, the TTA was decreased from 4.68 to 3.74 (sec) with vision. Normally, a small drifting bias is difficult to detect because the IM process uses the full-set filter solution which also slowly drifts. The proposed IM reset mechanism, which does not rely on the drifting current navigation solution, improves the detectability of a ramp fault.

5. CONCLUSION

This paper proposed the tightly-coupled Vision/GNSS navigation system for aircraft final approach. A time-delayed EKF framework, which performs a back-propagation forward in time by making use of image-trigger signals, has been established and applied to the navigation filter design. Then, it was augmented with the IM function founded on the batch-realization of this time-delayed KF with the new IM reset mechanism. The proposed navigation system has evaluated in open-loop simulations with

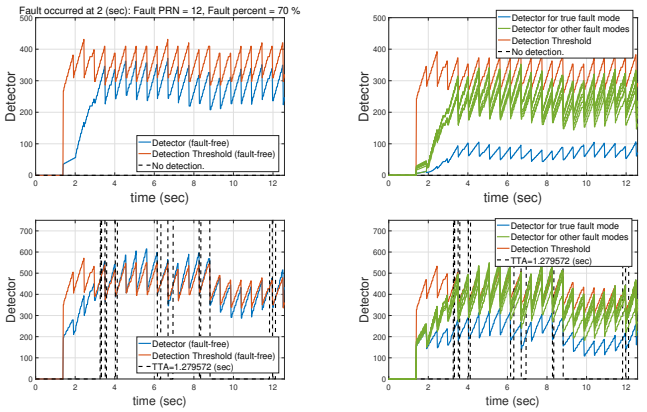

Fig. 8. Fault detector and threshold values of the full-set filter (left) and the sub-set filters (right) without (top) and with vision (bottom)

real sensor data acquired onboard the real UAV platform. The test results showed the improvement in fault detectability by adding onboard vision to the classical navigation sensor set. In future work, we would like to add a fault exclusion algorithm and make a closed-loop autonomous vision-based final approach with simulated GPS failure.

REFERENCES

C.Tonhäuser, A.Schwithal, S.Wolkow, M.Angermann, and P.Hecker (2015). Integrity concept for image-based automated landing systems. *ION Pacific PNT Meeting*.

ICAO (2005). Global navigation satellite system (gnss) manual. Doc 9849(AN/457).

L.Coutard, F.Chaumette, and J.M.Pflimlin (2011). Automatic landing on aircraft carrier by visual servoing. *IEEE International Conference on Intelligent Robots and Systems*.

M.E.Kügler, N.C.Mumm, F.Holzapfel, A.Schwithal, and M.Angermann (2019). Vision-augmented automatic landing of a general aviation fly-by-wire demonstrat. *AIAA SciTech Forum*.

M.Joerger and B.Pervan (2013). Kalman filter-based integrity monitoring against sensor faults. *AIAAJournal of Guidance Control and Dynamics*, 36(2).

M.Joerger, F.C.Chan, and B.Pervan (2014). Solution separation versus residual-based raim. *NAVIGATION: Journal of The Institute of Navigation*, 61(4).

T.D.Larsen, N.A.Andersen, O.Ravn, and N.K.Poulsen (1998). Incorporation of time delayed measurements in a discrete-time kalman filter. *IEEE Conference on Decision and Control*.

T.Goncalves, J.Azinheira, and P.Rives (2010). Homographie-based visual servoing of an aircraft for automatic approach and landing. *IEEE International Conference on Robotics and Automation*.

V.Gibert, L.Burlion, A.Chriette, J.Boada, and F.Plestan (2015). Nonlinear observers in vision system: Application to civil aircraft landing. *IEEE European Control Conference*.

Y.Watanabe, A.Manecy, A.Hiba, S.Nagai, and S.Aoki (2019). Vision-integrated navigation system for aircraft final approach in case of gnss/sbas or ils failures. *AIAA SciTech Forum*.